Fragment emission from the mass-symmetric reactions ^{58}Fe,^{58}Ni + ^{58}Fe,^{58}Ni at E_{beam} = 30 MeV/nucleon

E. Ramakrishnan, H. Johnston, F. Gimeno-Nogues, D. J. Rowland, R. Laforest, Y-W. Lui, S. Ferro, S. Vasal, and S. J. Yennello

Cyclotron Institute, Texas A & M University, College Station, Texas 77843

(Received 9 July 1997)

The mass-symmetric reactions ^{58}Fe,^{58}Ni + ^{58}Fe,^{58}Ni were studied at a beam energy of E_{beam} = 30 MeV/nucleon in order to investigate the isospin dependence of fragment emission. Ratios of inclusive yields of isotopic fragments from hydrogen through nitrogen were extracted as a function of laboratory angle. A moving source analysis of the data indicates that at laboratory angles around 40° the yield of intermediate mass fragments (IMF's) beyond $Z=3$ is predominantly from a midrapidity source. The angular dependence of the relative yields of isotopes beyond $Z=3$ indicates that the IMF's at more central angles originate from a source which is more neutron deficient than the source responsible for fragments emitted at forward angles. The charge distributions and kinetic energy spectra of the IMF's at various laboratory angles were well reproduced by calculations employing a quantum molecular-dynamics code followed by a statistical multifragmentation model for generating fragments. The calculations indicate that the measured IMF's originate mainly from a single source. The isotopic composition of the emitted fragments is, however, not reproduced by the same calculation. The measured isotopic and isobaric ratios indicate an emitting source that is more neutron rich in comparison to the source predicted by model calculations. [S0556-2813(98)05904-4]

PACS number(s): 24.10.−i, 25.70.Lm, 24.10.Pa

I. INTRODUCTION

The study of fragment emission from heavy-ion collisions at intermediate and high energies provides us with the means to investigate nuclear matter under conditions of energy and density far removed from the ground-state configuration. The phenomenon of multifragmentation wherein fragments with charge greater than $Z=3$ are emitted with large multiplicities from heavy-ion reactions has been the focus of many measurements [1]. Some of the central issues that surround the multifragmentation process are the attainment of thermal and chemical equilibrium of hot nuclear matter prior to the production of fragments, and the dynamics and time scales involved in the fragment emission process. A vast majority of the measurements in this field have concentrated on the issue of the fragmentation dynamics and time scales, and on the question of thermal equilibration. With the advent of radioactive beam facilities, the influence of the isospin degree of freedom in heavy-ion collisions is being addressed [2]. The isospin degree of freedom thus becomes an important probe in the study of the dynamical aspects of the formation and decay of hot nuclear matter in heavy-ion collisions [3].

Previous measurements of fragment emission with isotopic resolution from very mass-asymmetric reactions of light ions on heavy targets of varying isotopic composition displayed that the N/Z ratio of the target is reflected in the N/Z composition of the intermediate mass fragments (IMF's) emitted in such reactions [4–6]. Such measurements were recently extended to less mass-asymmetric heavy-ion reactions [7]. In these measurements, a transition was observed in the emission of fragments, from a regime where the N/Z degree of freedom was equilibrated prior to emission at a lower beam energy, to a regime where the N/Z degree of freedom was not equilibrated prior to emission at a higher beam energy.

Another recent study of fragment emission in heavy-ion reactions of ^{124,136}Xe+^{112,124}Sn observed from the isospin composition of light charged particles that light fragments from a midvelocity region were substantially more neutron rich when compared to fragments from the projectile velocity region [8]. It was suggested that the fragments were emitted from the rupture of neutron-rich necklike structures formed in these heavy-ion reactions. Recent model calculations have demonstrated the evidence for neutron-rich neck regions [9], and evidence for the dependence of the N/Z ratio of the neck region on the isospin composition of the entrance channel [10]. In this work we present data and model calculations for IMF emission from the mass-symmetric reactions of ^{58}Fe,^{58}Ni + ^{58}Fe,^{58}Ni.

On the theoretical front, much progress has been made in the development of models that treat the formation of hot nuclear matter in heavy-ion collisions in a dynamical way. Model calculations based on the quantum molecular-dynamics (QMD) approach [11] and the Boltzmann-Uehling-Uhlenback (BUU) mean-field approach [12] have been developed and utilized to describe the reaction dynamics in heavy-ion collisions at intermediate energies. The isospin degree of freedom has been introduced into the BUU model by accounting for the difference in the nucleon-nucleon scattering cross section and in the nuclear potential [12]. Though these models take into account the dynamics in the collisional phase of the reactions, the calculations themselves do not directly yield fragments to be compared with measured data. These calculations are carried out to a certain time step in the reaction, resulting in a distribution of nucleons. A second stage of the calculation involves identifying excited clusters and free nucleons from this distribution, and subsequently the decay of the identified hot clusters to nuclear fragments based on the assumption of thermal and statistical equilibrium. The measurement of fragments with

isotopic resolution from heavy-ion collisions should thus provide a sensitive tool to study the validity of the assumptions made in the dynamical and statistical stages of these model calculations.

II. EXPERIMENTAL DETAILS

The experiments were performed at the Cyclotron Institute in Texas A&M University (TAMU). Self-supporting isotopically enriched targets of ^{58}Fe (2.3 mg/cm^2) and ^{58}Ni (1.75 mg/cm^2) were bombarded by isotopic beams of ^{58}Fe and ^{58}Ni from the K500 Superconducting Cyclotron at a beam energy of 30 MeV/nucleon. The targets were placed in the center of a scattering chamber that was housed inside the TAMU 4π neutron ball detector [13]. Fragments from the reaction were measured in six discrete particle telescopes placed inside the scattering chamber and centered at laboratory angles of 10°, 44°, 72°, 100°, 128°, and 148° [14]. Each telescope consisted of a gas ionization chamber (IC) followed by a pair of silicon detectors (Si-Si) and a CsI scintillator detector thus providing three distinct detector pairs (IC-Si, Si-Si, and Si-CsI) for fragment identification. The ionization chamber was of axial field design and was operated with CF_4 gas at 50 Torr. The gaseous medium was 6 cm thick and typical thresholds were $\sim$0.5 MeV/nucleon for intermediate mass fragments. The silicon detectors had an active area of 5 cm $\times$ 5 cm and were each subdivided into four quadrants. The first and second silicon detectors in the stack were 0.14 mm and 1 mm thick, respectively. The dynamic energy range of the silicon pair was $\sim 16-50$ MeV for ^{4}He and $\sim 90-270$ MeV for ^{12}C. The CsI scintillator crystals that followed the silicon detector pair were 2.54 cm in thickness and were read out by photodiodes.

Good Z identification was achieved for fragments that punched through the IC detector but were stopped in the first silicon detector. Fragments were measured in the Si-Si detector pair with very good isotopic separation. The Si-CsI detector provided good isotopic separation of light charged particles up to ^{4}He. The telescopes were oriented such that the quadrant silicon detectors provided two distinct angular bites of coverage for each telescope. For instance, the telescope placed at 44° provided two angular ranges of 8° each, centered at angles of 40° and 48°.

The IC-Si detector pair was calibrated with α-emitting sources by operating the IC at different gas pressures. The Si-Si pair was calibrated by measuring the energy deposition of α particles from radioactive sources in the thin silicon, and by the punch-through energy point for various isotopes in the thick silicon. The Si-CsI detector pair was calibrated by choosing points along different light charged isotope lines and then determining the energy deposition in the CsI crystal from the energy loss in the calibrated Si detector.

III. ISOTOPIC YIELDS OF EMITTED FRAGMENTS

Fragments beyond lithium were measured copiously only in the telescopes placed at 10° and 44°. The measured kinetic energy spectra for various Z's exhibited typical exponential shapes, and are presented in a later section of the paper. In this section we look at the inclusive yields of fragments with isotopic resolution from the Si-Si detector pair at various laboratory angles.

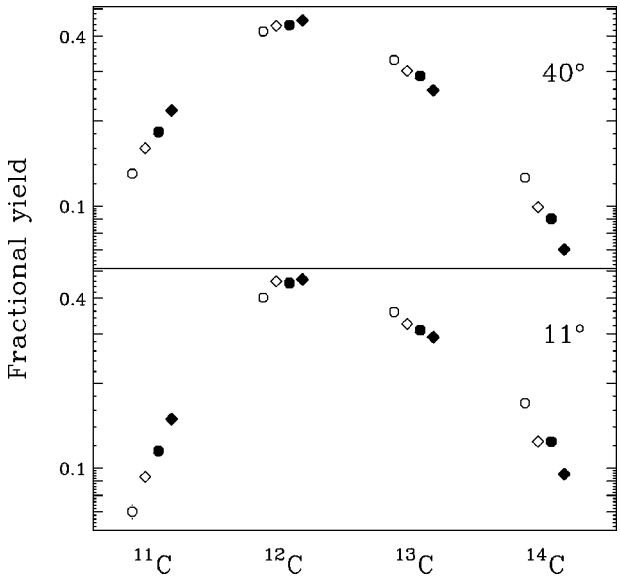

FIG. 1. Fractional yields of ^{11}C through ^{14}C isotopes to the total yield of all carbon isotopes measured in the Si-Si detector pairs at laboratory angles of 11° and 40° from the reactions ^{58}Fe+^{58}Fe (open circles), ^{58}Fe+^{58}Ni (open diamonds), ^{58}Ni+^{58}Fe (filled circles), and ^{58}Ni+^{58}Ni (filled diamonds). Error bars are smaller than the symbols.

Figure 1 displays the fractional yields of ^{11}C through ^{14}C isotopes to the total yield of all carbon isotopes at laboratory angles of 11° and 40° from the four reactions Fe+Fe (open circle), Fe+Ni (open diamond), Ni+Fe (filled circle), and Ni+Ni (filled diamond). Here, Fe+Ni represents the reaction of ^{58}Fe projectile on ^{58}Ni target. This notation is used throughout the paper. The relative yields display a dependence on the overall isospin composition in the entrance channel. For instance, the relative yield of ^{11}C fragments from the Fe+Fe reaction is much less than the yield from the Ni+Ni reaction. This could be linked to the entrance channel in that the Ni+Ni reaction has more protons than the Fe+Fe reaction thus producing more of the neutron-deficient species of carbon isotopes. Furthermore, the relative yields from the Fe+Ni and the Ni+Fe reactions themselves are different for the ^{11}C isotope thereby indicating possible influence of the entrance channel dynamics in the composition of the emitting source.

From Fig. 1 it can be observed that the fractional yields of the various isotopes also depend on the measurement angle. This dependence is displayed in Fig. 2 for carbon, beryllium, and lithium isotopes. The fractional yields indicate that at more central angles, the fragments seem to have originated from a source that is more neutron deficient. This is indicated by the fact that the relative yield of ^{11}C increases with increasing laboratory angle whereas the yield of ^{14}C decreases. This behavior is prominent in the yields of heavier isotopes of beryllium through carbon and not prominent in the yields of lithium isotopes. The behavior of the lithium isotopes may indicate a transition to the regime where neutron-rich light isotopes were measured at these central angles [8].

In describing the angular dependence of isotopic yields, the influence of detector acceptance effects on the measured

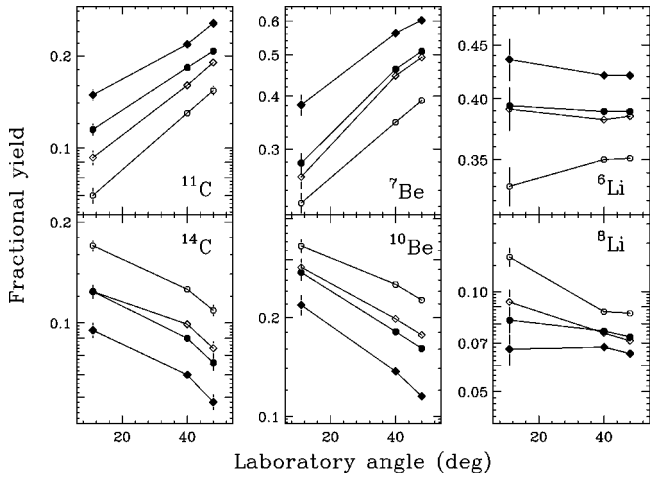

FIG. 2. Fractional yields of some carbon, beryllium, and lithium isotopes measured in the Si-Si detector pair as a function of laboratory angle from the four reactions. The symbols have the same meaning as in Fig. 1. The lines are drawn to guide the eye.

yield for fragments with varying mass needs to be considered. A simulation was performed by assuming a midrapidity source whose emission characteristics were obtained from the moving source fits described in a later section. The simulation reproduced well the kinetic energy spectra of the measured fragments in the Si-Si detector pair. The ratio of yields of ^{12}C to ^{11}C fragments emitted isotropically in the center-of-mass frame was derived from the simulation as a function of laboratory angle, folded with the acceptance of the Si-Si detector pairs and compared to the ratio derived from the measured yields. This comparison is displayed in Fig. 3. The simulation exhibits an angular dependence of the detector acceptance effect, but this dependence is rather small when compared to the data.

The ratios of inclusive yields of isotopic fragment pairs that differ by one neutron and isobaric fragment pairs that

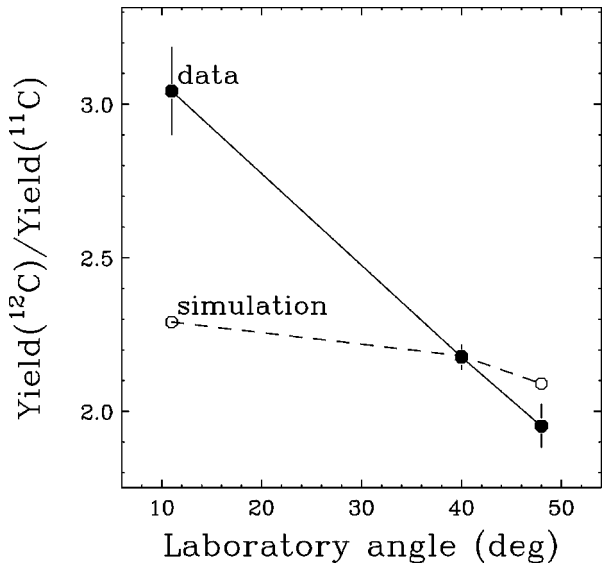

FIG. 3. Ratios of yields of ^{12}C to ^{11}C fragments from data (filled circles) and from a simulation (open circles) based on moving source fits are plotted as a function of laboratory angle. The simulation was normalized to the data at 40°.

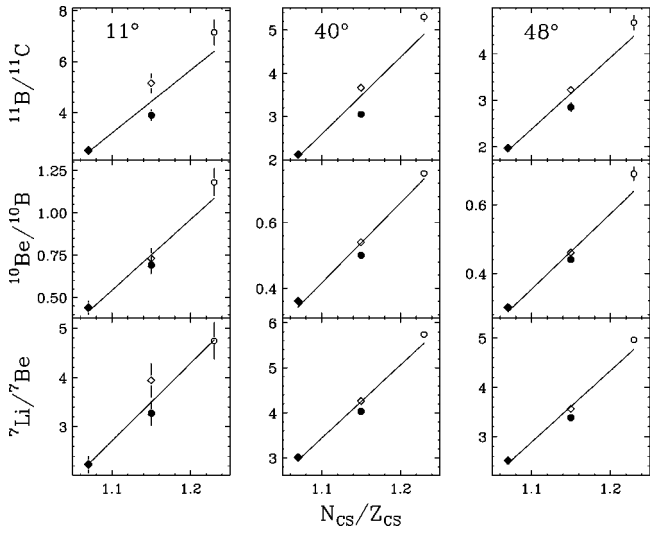

FIG. 4. Ratios of yields of isobaric pairs of nuclei measured in the Si-Si detector pairs from the four reactions plotted as a function of the ratio of the total number of neutrons (N_{CS}) to the total number of protons (Z_{CS}) in the entrance channel. The symbols represent the same reactions as in Fig. 1. The lines represent linear fits to the ratios from the four reactions.

differ by one charge unit, measured over their common range of energies in the Si-Si detector pair, were computed for various measurement angles. Figure 4 displays the ratio of relative yields of various isobaric pairs of fragments at the three laboratory angles of 11°, 40°, and 48°, as a function of the N/Z of the composite system in the entrance channel of the reaction. The ratios correspond to the yields for the more neutron-rich species of the isobar in comparison to the more neutron-deficient species. To first order, the ratios are a function of the N/Z of the composite system, indicating that the fragments originated from a source that had contributions from both projectile and target nuclei. Nevertheless, the ratios do not all fall on a single line. For instance the ratio of ^{11}B to ^{11}C from the Fe+Ni and Ni+Fe reactions do not overlap. This may be due to emission from a source that was not equilibrated in the N/Z degree of freedom. Also, contributions from multiple sources to the measured fragment yields, or the influence of differing Coulomb forces on the different charges of the two nuclei in each isobaric pair cannot be ruled out at this point.

The relative yields of fragment pairs of the same charge but differing in mass by one neutron are displayed in Fig. 5. Except in the case of the heavier carbon fragments, the ratios from the four reactions scale linearly as a function of the N/Z of the composite system in the entrance channel. Nevertheless contributions from multiple emission sources or variations in detection efficiency due to the different masses of the fragments in each isotopic pair cannot be discounted at this juncture. In summary, the isotopic and isobaric ratios of fragments measured at laboratory angles of 11°, 40°, and 48° scale approximately with the N/Z of the composite system in the entrance channel indicating that the fragments originated from a source or sources that had contributions from both projectile and target nuclei.

For the mass-symmetric reactions studied here, the laboratory angle of $\sim$40° corresponds to center-of-mass angles around 90°, and hence the contribution to intermediate mass

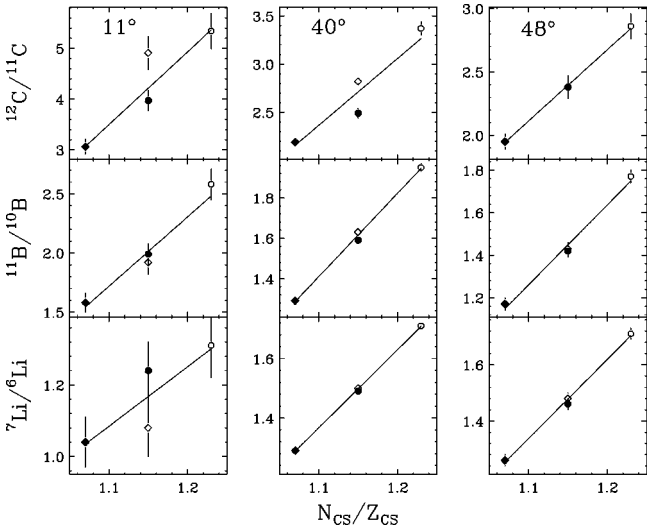

FIG. 5. Ratios of yields of isotopic pairs of nuclei measured in the Si-Si detector pairs from the four reactions plotted as a function of the N/Z of the composite system in the entrance channel. The symbols have the same meaning as in Fig. 1, and the lines represent linear fits to the ratios from all four reactions.

fragments from projectilelike and targetlike sources should be negligible. Calculations based on moving source fits described in the next section show that for a midrapidity source moving with a velocity of $0.1c$, the laboratory angle of 40° corresponds to center-of-mass angles of 80°–100° for ^{6}Li fragments and 68°–92° for ^{12}C fragments, over the energy range measured in the Si-Si detector pair. Previous studies of fragmentation at similar energies have demonstrated the use of neutron multiplicity as a centrality variable in heavy-ion reactions [15]. Measurements performed on mass 40 + mass 58 systems showed that neutron multiplicity provided an additional centrality condition over the restriction of angular range of fragment detection in the laboratory [7]. However for heavy, mass-symmetric reactions the measured neutron multiplicity could be less sensitive to impact parameter due to copious emission of neutrons at large impact parameters [16].

The neutron multiplicity in coincidence with fragments detected in the telescopes was derived from QMD and statistical multifragmentation model (SMM) calculations for impact parameters of 0–7 fm. Details of this calculation are presented in a later section. The calculated neutron multiplicity was filtered for detection geometry and detection efficiency of the neutron ball [17] and compared to the coincident neutron multiplicity measured in the experiment. The overall shape of the measured neutron multiplicity was roughly reproduced by the QMD-SMM calculation. However, the QMD-SMM calculation indicated that the mean multiplicity of neutrons is not very sensitive to the impact parameter. The average neutron multiplicity decreased from a value of 9.7 at an impact parameter of 1.5 fm to only 8.0 at 6.5 fm, and the overall shape of the multiplicity remained unchanged as a function of impact parameter. Thus according to the QMD-SMM calculations gating on higher neutron multiplicities in the data does not ensure a good centrality selection for these mass-symmetric reactions. Therefore comparison of the data with model calculations was performed only at the inclusive level.

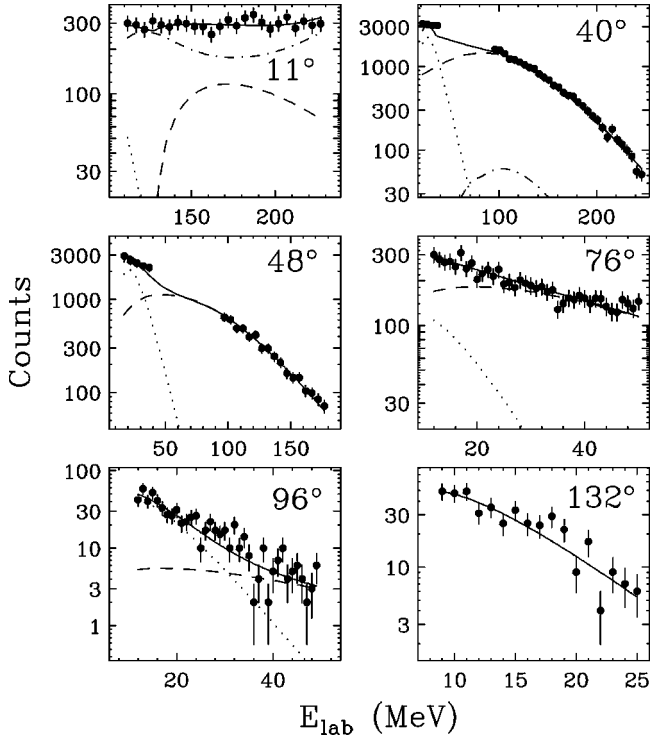

FIG. 6. Measured kinetic energy spectra compared to fits performed with a moving source analysis. The filled circles represent $Z=6$ fragments at laboratory angles of 11°, 40°, 48°, 76°, 96°, and $Z=4$ fragments at 132°. Contributions from the targetlike source (dotted line), the midrapidity source (dashed line), the projectilelike source (dot-dashed line), and the sum of all three contributions (solid line) are displayed.

IV. MOVING SOURCE ANALYSIS

The kinetic energy spectra of fragments measured at various laboratory angles were subject to a moving source analysis based on the work of Wile *et al.* [18], in order to determine the kinematics of the source or sources that contributed to the fragment yields.

At backward angles in the laboratory, the contribution to the kinetic energy spectra should be predominantly from an excited targetlike source. The spectra at the backward angle of 132° were thus fit with a targetlike source based on the scission point model of Nix and Moretto [18,19]. The source velocity and slope temperature were allowed to vary in the range of $0.01–0.04c$ and 3–10 MeV, respectively. Best fits for $Z=3$ and $Z=4$ spectra were obtained for a source velocity of $0.03c$ and a slope temperature of 6 MeV. The lower right panel of Fig. 6 displays the fit to the $Z=4$ kinetic energy spectrum at 132°.

For laboratory angles forward of 132°, the kinetic energy spectra were fit by a combination of three sources. The first source was the targetlike source, the parameters of which were fixed to the values determined by fits to the 132° data. The second source was modeled to be Maxwellian-like [18], with slope parameter and velocity varying in the range of 10–30 MeV and $0.1–0.14c$, respectively. The projectile and center-of-mass velocity in the laboratory frame for the reactions studied here were 0.25 and $0.125c$, respectively. The third source was a projectilelike source which was modeled similar to the targetlike source. The velocity of this source

TABLE I. Parameters extracted from the moving source analysis of the kinetic energy spectra. The source velocity β, the slope parameter T, and the fraction of Coulomb barrier are listed. Ranges indicate the values obtained by fitting spectra of $Z=3-6$ fragments over all laboratory angles. Single numbers represent fixed values assigned to the parameters in the fitting procedure. See text for details.

Parameter	Target	Midrapidity	Projectile
β (c)	0.03	0.10–0.13	0.17–0.23
T (MeV)	6.0	15.9–27.7	6.0
Frac. Coul.	0.1–0.99	0.1–0.95	0.14–0.99

was allowed to vary in the range of $0.19–0.22c$. Due to the mass symmetry in the entrance channel, the slope parameter for the projectilelike source was fixed at 6 MeV, which was the value obtained for the targetlike source. Allowing the projectile slope parameter to vary in the range of 3–10 MeV did not change the fits appreciably. The Coulomb term for the sources was set to a fraction of the value obtained on assuming two touching spheres. An additional parameter was used in the fitting procedure to determine this fraction.

The kinetic energy spectra for $Z=3–6$ fragments in the angular range of 11° to 96° were fit using the three-source description. The panels in Fig. 6 display the fit results for $Z=6$ fragments. It can be observed from the figure that the influence of the targetlike source diminishes as one moves to more forward angles in the laboratory, whereas the midrapidity source becomes more prominent. The projectilelike source has negligible contribution to the spectra except at 11°. At 40°, the yield in the energy range of the Si-Si detector pair is predominantly from the midrapidity source. At 11°, the yield is mostly from the projectilelike source, with some contribution from the midrapidity source. The parameters obtained from the source fits are summarized in Table I. Single numbers listed in the table correspond to fixed values assigned to the parameters, and ranges correspond to values extracted by fitting spectra of $Z=3–6$ fragments over the entire range of laboratory angles.

The moving source analysis thus indicates that at laboratory angles of $\sim 40°$, the inclusive kinetic energy spectra measured in the Si-Si fragment detector pair can be described by a single midrapidity source moving with a velocity close to that of the center of mass in the entrance channel.

V. MODEL CALCULATIONS

Calculations were performed with the dynamical codes BUU [12] and QMD [11] to simulate the mass-symmetric reactions studied here. Both BUU and QMD calculations follow the collisional dynamics at the nucleon-nucleon level. The BUU code had isospin dependence introduced in the nuclear potential as well as in the nucleon-nucleon collisional cross section. Both codes were executed from the beginning of the collision to a time step of 200 fm/c, for impact parameters in the range 0–7 fm. At the end of these dynamical calculations, the resulting nucleon distributions were input to a cluster search algorithm that identified hot residues and free nucleons. Subsequently the residues and the free nucleons were input to a calculation employing a statistical multifragmentation model (SMM) [20] that produced fragments from the hot residues. These fragments were transformed to the laboratory frame of reference, after applying multiparticle Coulomb tracking, and filtered for the angular and energy acceptance of the detectors.

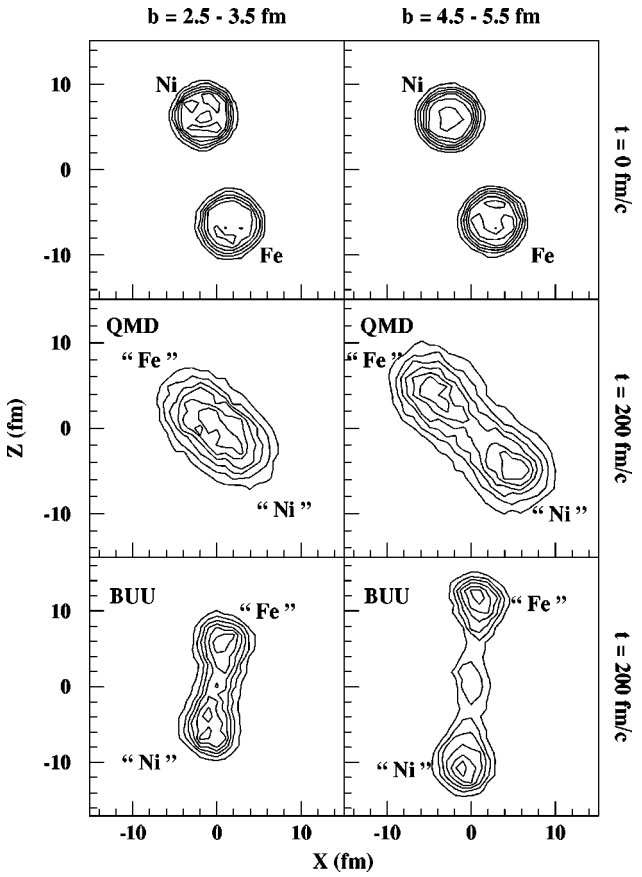

FIG. 7. Contour plots of nucleon distributions from QMD and BUU calculations performed for the reaction Fe+Ni. The left and right panels correspond to impact parameters of ~ 3 and ~ 5 fm, respectively. The top two panels correspond to a time of $t=0$ fm/c. The middle panels are from the QMD calculation at a time of 200 fm/c, and the bottom panels are from the BUU calculation at 200 fm/c.

Figure 7 displays contour plots of the nucleon distributions generated by QMD and BUU calculations for the reaction Fe+Ni for impact parameters of ~ 3 and ~ 5 fm at time steps of 0 and 200 fm/c. It can be observed that the two calculations result in rather different distributions of nucleons. The interaction in the case of QMD appears to be stronger than that of BUU. In the QMD calculation the nuclei stay close together longer to the extent that there is formation of a dinuclear compound system that possesses appreciable angular momentum. Furthermore, there appears to be more nuclear matter in the midrapidity region in the QMD calculation. The stiffness of the equation of state of nuclear matter could influence the formation of extended necklike structures in these reactions [9]. The BUU calculations were performed assuming a soft equation of state with an incompressibility constant of $K=200$ MeV. The QMD calculations employed here are not sensitive to nuclear incompressibility at least for this reaction energy [21].

Comparisons between the model calculations and mea-

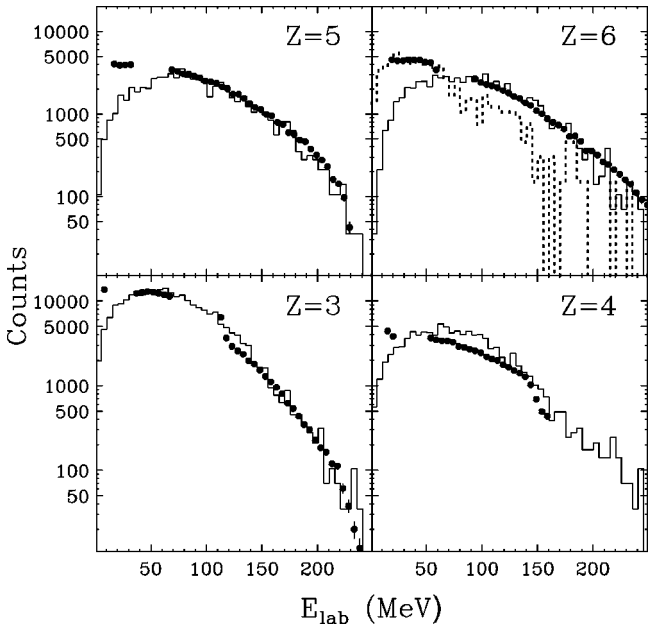

FIG. 8. Comparison of calculations (histograms) with measured kinetic energy spectra (filled circles) at the laboratory angle of 40° for $Z=3,4,5$, and 6. The discontinuity in the data points corresponds to the energy regime where the fragments punch through the IC-Si detector pair into the Si-Si detector pair. The solid histograms correspond to the QMD-SMM calculation which was normalized to the data for $Z=6$ in the energy range of 100 to 200 MeV. The dotted histogram in the upper right panel is from a BUU-SMM calculation which was normalized to the data at the lower energy range.

sured data were performed at the inclusive level. Figure 8 displays the kinetic energy spectra of fragments measured in the telescope at 40° in comparison to model calculations. The filled circles correspond to the data and the solid histograms correspond to QMD-SMM calculations. The dotted histogram in the top right panel corresponds to a BUU-SMM calculation. The QMD-SMM calculations describe the kinetic energy spectra rather well for all Z's even though it underpredicts the measurement at the low-energy end. The agreement in the energy range of the Si-Si detector pair is nevertheless very good. The BUU calculation shown for $Z=6$ reproduces the lower energy end of the spectrum, but fails to reproduce the higher energy range.

In Fig. 9, the charge distribution measured in the Si-Si detector pair at laboratory angles of 11°, 40°, and 68° are compared to QMD-SMM and BUU-SMM model calculations. Both calculations were normalized to the $Z=3$ data point at 40°. The solid histograms which correspond to the QMD-SMM calculations reproduce the distribution rather well at all three angles. The BUU-SMM calculations shown as the dotted histograms do not follow the data as closely, except at 68°. At 40° the BUU-SMM calculation falls off more rapidly than the data and at 11° it largely overpredicts the formation of light fragments.

The QMD-SMM calculations reproduce the kinematics and charge distribution rather well and so they were investigated further to provide insight into the reaction dynamics. Figure 10 displays the source distribution that is obtained from QMD after the clusterization routine and prior to the statistical multifragmentation calculation. The QMD calculation predicts a single source for impact parameters up to ~5 fm, and the contribution from events with two sources becomes significant only at ~6 fm.

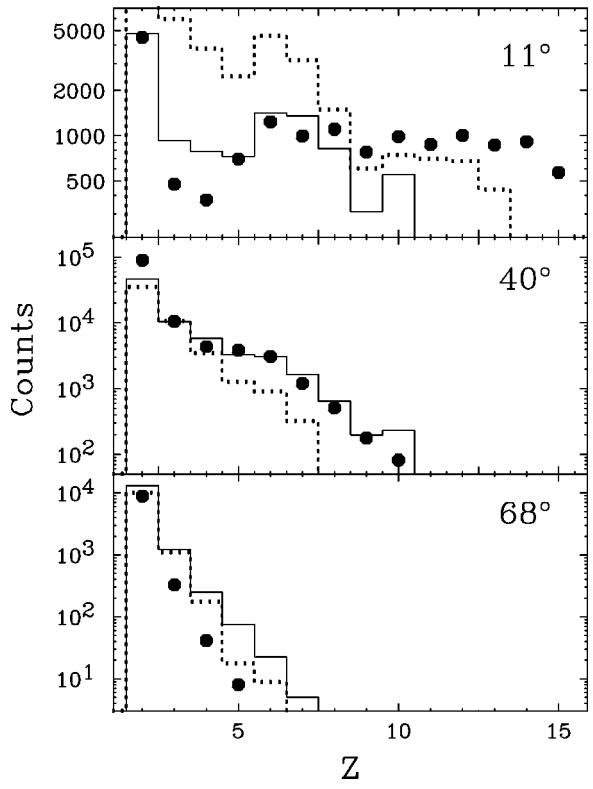

FIG. 9. The charge distribution measured in the Si-Si detector pair (filled circles) is compared to calculations performed using QMD-SMM (solid histogram) and BUU-SMM (dotted histogram) models at laboratory angles of 11°, 40°, and 68°. The calculations were normalized to the $Z=3$ data point at 40°. Error bars on data are smaller than the symbols.

The yields of $Z=2,3$ and $Z=4-6$ fragments at 11° (open circles) and 40° (filled circles) for the Si-Si detector pair as a

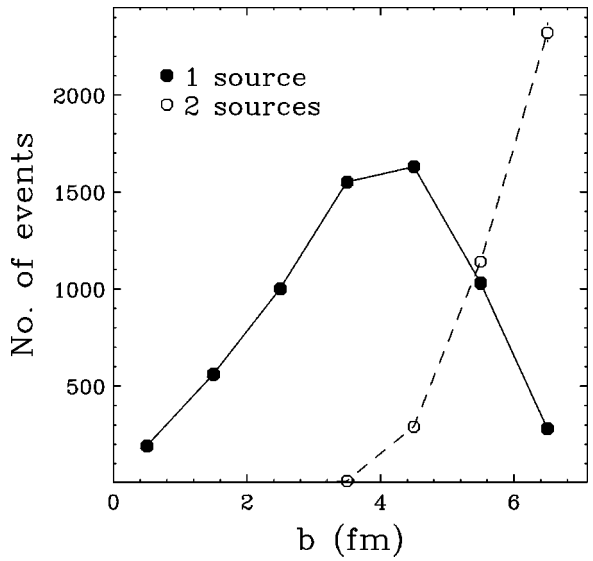

FIG. 10. The distribution of sources after the QMD calculation has been subject to the cluster search algorithm, as a function of impact parameter. The filled circles correspond to events that resulted in a single source and the open circles to events that produced two sources.

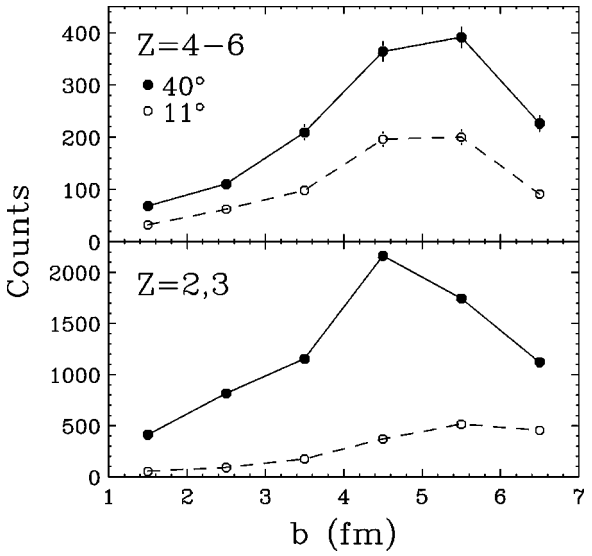

FIG. 11. The yields of $Z=2,3$ and $Z=4-6$ fragments at 11° (open circles) and 40° (filled circles) predicted by QMD-SMM calculations for the Si-Si detector pair, as a function of impact parameter. The error bars represent statistical errors in the calculation.

function of impact parameter as predicted by the QMD-SMM calculations are displayed in Fig. 11. For the lighter fragments the calculations predict yields at 11° that do not change appreciably at larger impact parameters. But for the IMF's, the yield at 11° drops off sharply after an impact parameter of ~5 fm. For the 40° angle, the yield of lighter fragments and IMF's both drop off at the highest impact parameters. Though the yield of heavy fragments increases with impact parameter for the two-source events, the contribution from two-source events to the total yield of IMF's with $Z=3-6$ is of the order of 10–20 %.

Figure 12 displays the ratio between the yields of fragments at 11° to fragments at 40° in the laboratory from the

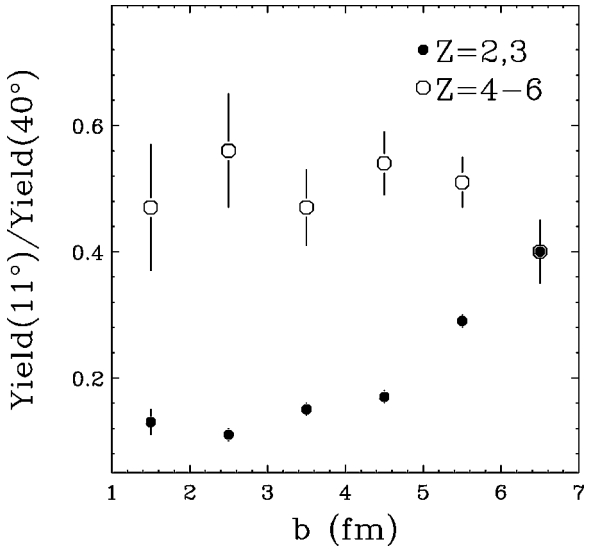

FIG. 12. The ratio of yields of $Z=2,3$ (filled circles) and $Z=4-6$ (open circles) fragments at 11° to 40° predicted by QMD-SMM calculations for the Si-Si detector pair, plotted as a function of the impact parameter. The error bars represent statistical errors in the calculation.

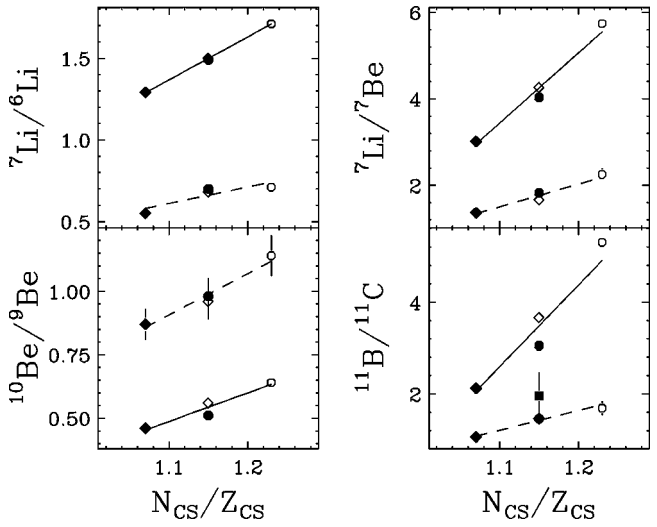

FIG. 13. Yield ratios of isotopic and isobaric pairs of fragments from QMD-SMM calculations (symbols joined by dashed lines) in comparison with ratios from measured data (symbols joined by solid lines) at the laboratory angle of 40°. The symbols represent the four reactions in the same order as in Fig. 1. The lines are first-order fits to the ratios for both data and calculations. The additional point represented by the filled square in the bottom right panel is from a BUU-SMM calculation.

QMD-SMM calculation, filtered for the Si-Si detector pair. The filled circles represent the yield ratio for $Z=2,3$ fragments and the open circles represent the $Z=4,5$, and 6 fragments. It is seen clearly that for the lighter fragment group, there is more contribution at forward angles at large impact parameters, which is expected from a projectilelike source that would result from peripheral collisions. For the IMF's the ratio is rather constant with increasing impact parameter indicating that at the two angles the IMF's originate from similar sources. Thus, in the QMD-SMM calculations the yields of fragments beyond $Z=3$ arise mainly from impact parameters up to ~5 fm where there is predominantly only one hot residue predicted by the calculation.

It was observed in the QMD-SMM calculations that IMF's beyond $Z=3$ were not present in the output from QMD, and were only produced in the statistical stage of the calculation. In other words, intermediate mass fragments like ^{11}C were found to be emissions in the statistical stage, and were not found as residues at the end of the dynamical stage. It was therefore verified independently that the isotopic composition of fragments emitted from the SMM calculation scaled with the N/Z composition of the source input to the SMM stage. The QMD calculation did not have explicit isospin dependence incorporated into the nucleon-nucleon collisional dynamics. Therefore the isospin dependence that is predicted by the calculations may just be a function of the total number of protons and neutrons present in the entrance channel.

With the above-mentioned points under consideration, ratios of isotopic and isobaric yields generated by the QMD-SMM calculation were compared to the ratios from the measurements that were presented earlier. Figure 13 displays the yield ratios of isotopic pairs that differ by one neutron and isobaric pairs that differ by one charge unit for four pairs of nuclei at the laboratory angle of 40°. The symbols joined by

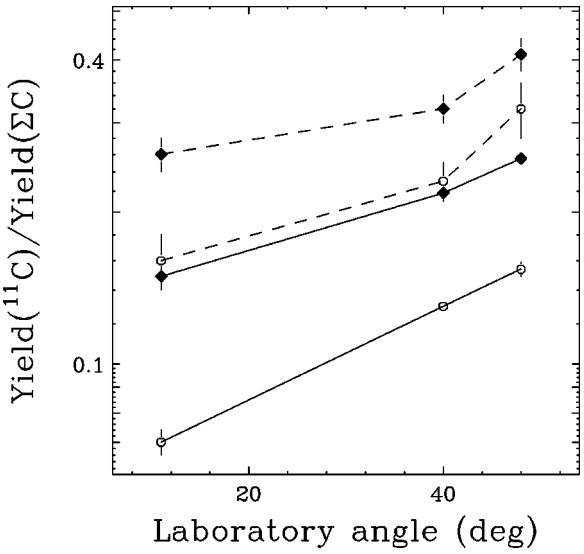

FIG. 14. Ratio of relative yield of ^{11}C to all carbon fragments in the Si-Si detector pair from QMD-SMM calculations (symbols joined by dashed lines), in comparison to the ratio from the measured data (symbols joined by solid lines) plotted as a function of the laboratory angle for the two reactions Fe+Fe (open circles) and Ni+Ni (filled diamonds). The lines are drawn to guide the eye.

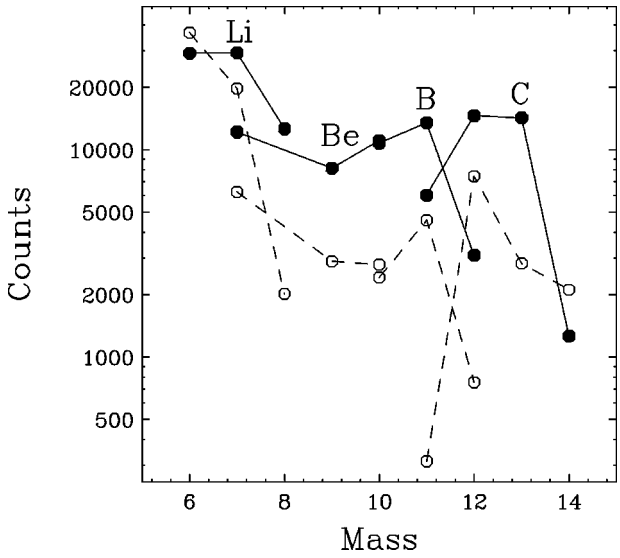

FIG. 15. Fragment yields for isotopes of Li, Be, B, and C from SMM (filled circles and solid lines) and GEMINI (open circles and dashed lines) calculations, generated from a source distribution produced by QMD for the Fe+Fe reaction. The lines are drawn to guide the eye.

the solid line represent ratios derived from the inclusive yields measured in the Si-Si detector pair, presented earlier. The symbols joined by the dashed lines are derived from the QMD-SMM calculation for impact parameters of 0–7 fm. It can be observed that the calculations can be fit by a single line as a function of the N/Z of the composite system. The ratios of yields from the Fe+Ni and Ni+Fe reactions that have the same N/Z for the composite system overlap well in the calculations. Overall, the calculated ratios underpredict the measured ratios by a large margin, except for the ^{10}Be/^{9}Be ratio. It was observed that ratios involving ^{10}Be behaved differently than others ratios implying that the relative yield of ^{10}Be from the calculation is very different compared to the actual measurement. The filled square in the bottom right panel represents the ratio of ^{11}B to ^{11}C from a BUU-SMM calculation. This calculation, which did not reproduce the charge and kinetic energy distribution of the fragments very well, also underpredicts the data and is similar to the predictions of the QMD-SMM calculation for this isobaric pair. The angular dependence of the relative yield of ^{11}C to all carbon fragments from the QMD-SMM calculation is compared to data in Fig. 14 for the two reactions Fe+Fe and Ni+Ni. It is seen that though the overall trend of the relative yield as a function of laboratory angle is well reproduced, the calculated values are rather different from the measured data.

Comparisons with the data thus indicate that the measured fragments result from a source that is substantially more neutron rich than that predicted by the model calculations. The possible influence of the emission of small symmetric clusters such as α particles on the N/Z composition of the source that emitted the heavy intermediate mass fragments cannot be ruled out [22]. The neutron richness of the emitting source could be enhanced by the emission of such symmetric light clusters in the early stages of the reaction. Due to the lack of centrality information, and due to the absence of complete kinematic information on emitted neutrons and other light charged particles, this issue could not be addressed using the present data set.

Further analysis of the free particle and fragment distributions from the calculation for the Fe+Ni reaction show that at the end of the dynamical stage (QMD) of the calculation, the residues identified by the cluster search process have the same N/Z ratio as the entrance channel. At this point, 5.7% of the neutrons and 6.2% of the protons in the entrance channel are in the form of free nucleons. Including the light clusters of d, t, ^{3}He, and ^{4}He changes these numbers to 6.1 and 6.8% for neutrons and protons, respectively. After the statistical stage, 22.7% of the neutrons and 18.6% of the protons are found as free nucleons. The numbers change to 27.2 and 23.7% respectively for neutrons and protons on including light clusters. Thus a large fraction of the entrance channel nucleons are found to be free or bound in light clusters in these calculations. The fraction of neutrons exceeds that of the protons, which is qualitatively consistent with the increased yield of proton-rich fragments in the calculation when compared to the measured data.

The calculations nevertheless predict that the source becomes less neutron rich at more central angles, consistent with the data. These observations raise the issue as to how the isotopic composition of emitted fragments is influenced by the statistical stage of the calculations after the formation of the hot residue in the dynamical stage. In order to address this issue, a comparative calculation was performed using the SMM and GEMINI [23] models. The charge, mass, and excitation energy distributions for events that resulted in a single source from a QMD calculation of the reaction Fe+Fe were input to the two after burner codes of SMM and GEMINI. The total yields of various isotopes of Li, Be, B, and C from the two after burner calculations are displayed in Fig. 15. Overall, it is seen that the GEMINI calculation (open circles) produces less yield than the SMM calculation (filled circles) for fragments heavier than ^{6}Li. Though the overall

shape of the yield curves from both calculations are rather similar, there are significant differences. For instance, the ratio of ^{11}C to ^{11}B fragments is drastically different between SMM (ratio$=2.23\pm0.03$) and GEMINI (ratio$=14.53\pm1.20$) because the yield of ^{11}C fragments is largely underpredicted by GEMINI in comparison to SMM.

Thus the comparison of yield ratios of isotope/isobar pairs can be strongly influenced by the after burner stage of the model calculations. Furthermore, the discrepancy between the measured and calculated yield ratios may also have been influenced by the loss of reaction dynamical information on coupling the nucleon distribution generated by QMD with the statistical stage of the SMM model.

VI. CONCLUSIONS

The mass-symmetric reactions of ^{58}Fe, ^{58}Ni + ^{58}Fe, ^{58}Ni were measured in order to investigate the influence of the isospin of the entrance channel in the emission of intermediate mass fragments. The yield ratios of isotopic and isobaric pairs of fragments measured at laboratory angles of $\sim40°$ indicate that the isospin composition of the IMF's is a function of the entrance channel isospin, thereby indicating that the fragments were emitted from a reaction zone that had contributions from both target and projectile nuclei. A moving source analysis of the measured kinetic energy spectra demonstrated that at $\sim40°$ in the laboratory frame, the fragments originated from a midrapidity source moving with a velocity close to that of the center-of-mass velocity in the entrance channel.

The heavy-ion collision dynamics were modeled with a QMD calculation and a BUU calculation, followed by a fragment emission code based on the SMM model. The QMD-SMM calculations reproduced the observed charge and kinetic energy distribution very well for fragments detected in the Si-Si detector pair, whereas the BUU-SMM calculation did not reproduce the measured data very well. The QMD-SMM calculations are in agreement with the moving source analysis in predicting that the fragments measured at $\sim40°$ in laboratory arise predominantly from a single midrapidity source. Though the charge and kinetic energy distributions from the measurement were well reproduced by the QMD-SMM calculations, the observed ratios of isotopic and isobaric fragment yields were not well reproduced. Comparisons with the data suggest that the source emitting the IMF's measured in the midrapidity region is substantially more neutron rich than that predicted by the model calculations. This discrepancy may have been influenced by the assumptions made in coupling the dynamical stage of the calculations to the statistical stage, as well as the mechanism of fragment production in the statistical stage of the calculations. A good dynamical model that accounts for isospin dependence and for the dynamical formation and emission of intermediate mass fragments is necessary in order to interpret the isospin composition of fragments measured in heavy-ion reactions.

ACKNOWLEDGMENTS

This work was partially supported by the U.S. National Science Foundation under Grant No. PHY-9457376 and by the Department of Energy under Grant No. 93ER40773 and the Robert A. Welch Foundation under Grant No. A-1266.

[1] L. G. Moretto and G. J. Wozniack, Annu. Rev. Nucl. Part. Sci. **43**, 123 (1993).
[2] Bao-An Li, C. M. Ko, and W. Bauer, Int. J. Mod. Phys. E **7**, 1 (1998).
[3] S. J. Yennello *et al.*, Phys. Lett. B **321**, 15 (1994).
[4] R. Wada *et al.*, Phys. Rev. Lett. **58**, 1829 (1987).
[5] F. Deak, A. Kiss, Z. Seres, A. Galonsky, and L. Heilbronn, Phys. Rev. C **43**, 2432 (1991).
[6] J. Brzychczyk, D. S. Bracken, K. Kwiatkowski, K. B. Morley, E. Renshaw, and V. E. Viola, Phys. Rev. C **47**, 1553 (1993).
[7] H. Johnston *et al.*, Phys. Lett. B **371**, 186 (1996); Phys. Rev. C **56**, 1972 (1997).
[8] J. F. Dempsey *et al.*, Phys. Rev. C **54**, 1710 (1996).
[9] L. G. Sobotka, Phys. Rev. C **50**, R1272 (1994).
[10] M. Ditoro (private communication).
[11] J. Aichelin, G. Peilert, A. Bohnet, A. Rosenhauer, H. Stocker, and W. Greiner, Phys. Rev. C **37**, 2451 (1988); J. Aichelin, Phys. Rep. **202**, 233 (1991).
[12] Bao-An Li and S. J. Yennello, Phys. Rev. C **52**, R1746 (1995).
[13] R. P. Schmitt *et al.*, Nucl. Instrum. Methods Phys. Res. A **354**, 487 (1995).
[14] T. C. White *et al.*, Progress in Research, 1993-1994, Cyclotron Institute, TAMU, p. 146 (1994).
[15] J. Galin and U. Jahnke, J. Phys. G **20**, 1105 (1994); W. Skulski *et al.*, Phys. Rev. C **53**, R2594 (1996); J. Toke *et al.*, *Advances in Nuclear Dynamics 2*, edited by W. Bauer and G. D. Westfall (Plenum, New York, 1996).
[16] G. J. Kunde *et al.*, Phys. Rev. C **55**, R990 (1997).
[17] B. Hurst and R. P. Schmitt, Progress in Research, 1993-1994, Cyclotron Institute, TAMU, p. 147 (1994).
[18] J. L. Wile *et al.*, Phys. Rev. C **45**, 2300 (1992).
[19] J. R. Nix, Ann. Phys. (N.Y.) **41**, 52 (1967); L. G. Moretto, Nucl. Phys. **A247**, 211 (1975).
[20] J. P. Bondorf *et al.*, Phys. Rep. **257**, 133 (1995).
[21] K. Hagel *et al.*, Phys. Rev. C **50**, 2017 (1994).
[22] J. Randrup and S. E. Koonin, Nucl. Phys. **A356**, 223 (1981).
[23] R. J. Charity *et al.*, Nucl. Phys. **A483**, 371 (1988).